



Enhanced energy transport in high-mass flow solar parabolic trough collectors using Fe₂O₃-laden nanofluids

Rishikesh Kumar¹ · M. A. Hassan¹

Received: 23 April 2023 / Accepted: 14 September 2023 / Published online: 25 October 2023
© Akadémiai Kiadó, Budapest, Hungary 2023

Abstract

This study investigates an improved energy transport fluid for high-mass flow solar parabolic trough collectors. Fe₂O₃ nanoparticle-laden water-based nanofluids with various concentrations were studied, covering Reynolds numbers from 3×10^4 to 2.6×10^5 . Heat transfer coefficient, Nusselt number, and friction factor were analyzed and compared to the base fluid. A performance evaluation criterion is employed to assess the benefits. Notably, a significant enhancement in energy transport and performance evaluation was observed. Specific heat of nanofluids decreased due to nanoparticles, while thermal conductivity notably increased. Viscosity slightly increased. Doping with Fe₂O₃ nanoparticles led to decreased specific heat, increased thermal conductivity and viscosity. At flow rate of 1.5 kg s^{-1} , nanofluid exhibited 49.21% higher surface heat transfer coefficient for 0.5% nanoparticle concentration that goes up to 57.97% 1.0%. The average Nusselt number and the performance evaluation criterion also increase with nanoparticle concentration in nanofluid and Reynolds number. Correlations for heat transfer coefficient, friction factor, and Nusselt number were proposed as a function of Reynolds number and nanoparticle concentration.

Keywords Heat transfer · Nanofluid · Solar parabolic trough collector (SPTC) · NPs · Performance evaluation criterion (PEC)

List of symbols

FPCs	Flat plate collectors
CPCs	Compound parabolic collectors
PTCs	Parabolic trough collectors
C_R	Concentration ratio
A_p	Aperture area
A_r	Absorber tube area
SPTC	Solar parabolic trough collector
Nu_x	Local Nusselt number
NF	Nanofluid
base fluid	Base fluid
NPs	Nanoparticles
k_f	Thermal conductivity
ρ	Density
C_p	Specific heat
μ	Viscosity
ϕ	Volume concentration of nanoparticles

PEC	Performance evaluation criterion
h	Heat transfer coefficient
Nu	Nusselt number
f	Friction factor
HTF	Heat transfer fluid
Re	Reynolds number
lpm	Liters per minute

Introduction

Due to the mitigation of conventional energy resources, the burgeon in pollution, and hence the boom in the carbon footprint, researchers have shifted their interest toward alternative energy resources. Mitigation of fossil fuel reserves, air pollution, increasing electrical costs, and global warming can be controlled by reducing carbon footprints. Solar energy plays a pivotal role in the domain of renewable energy sources due to its ample availability.

A solar collector is an arrangement that converts solar radiation into heat, which is further transferred and utilized. Flat plate collectors (FPCs), compound parabolic collectors (CPCs), parabolic trough collectors (PTCs), Fresnel

✉ M. A. Hassan
hassan.me@nitjsr.ac.in

¹ Nano Fluid Laboratory, Department of Mechanical Engineering, National Institute of Technology Jamshedpur, Jamshedpur, Jharkhand 831014, India

lens concentrating collectors, etc., are most commonly used types of solar collectors [1]. The thermal efficiency of these collectors is inherited by their concentration ratio (C_R), which is the ratio of the aperture area (A_p) to the surface area of the absorber tube (A_r) [2]. FPC is used domestically because of its low-temperature output range (120–140 °C). For a high-temperature output (350–400 °C), the parabolic trough collector (PTC) is the most suitable contender among available solar collectors in which the thermal losses are relatively lower than the other collectors [3]. Solar parabolic trough collector (SPTC) is one of the most promising types of collectors. Air, water, oil, organic solvents, etc., are typical working fluids incorporated with these solar collectors [4]. The thermal performance behavior of PTC was first investigated by Arinze et al. [5] using water as a working fluid. A dynamic computer program was developed, and the thermal performance of water storage systems under varying charging and discharging circumstances was determined. A detailed one-dimensional heat transfer analysis on the SPTC was presented by Padilla et al. [6] by dividing the receiver tube into several segments. Collector efficiency and heat losses were computed under different operating conditions. A similar study for long and short receiver tubes was carried out by Forristall [7]. As solar collectors experience thermal losses, a method to reduce the thermal losses was reported by Ratzel et al. [8]. A two-dimensional unified numerical model for the coupled heat transfer process in the SPTC, including all modes of heat transfer, is nicely covered in the literature [9]. The various performance parameters and effects of the temperature field, flow field, local Nusselt number (Nu_x), and local temperature gradient were examined. An extensive review of PTC's modeling, simulation, and thermal performance investigation was nicely covered in the literature presented by Yilmaz et al. [10]. A detailed discussion about the single- and two-phase analysis based on steady and transient states was presented. Further, novel PTC designs and active and passive efficiency intensification techniques were deliberated collectively.

These collectors have relatively low outlet temperatures and poor efficiency that can be addressed by improving the thermal properties of the heat transport medium. Nanofluids (NFs) are assumed to have superior thermal and optical properties compared to base fluid and can be a suitable candidate for collectors to enhance their thermal performance [11]. Choi and Eastman [12] were the first to define a nanofluid (NF). Any base fluid, either organic or inorganic, with solid nanoparticles (NPs) of size 1–100 nm suspended in it is called nanofluids [13]. It has superior thermal properties, and hence heat transfer rate increases anomalously.

Regarding this, the first theoretical model was given by Maxwell [14], in which he added some micron-sized solid particles to the base fluid to increase the thermal conductivity (k_f). The heat transfer capability of NF depends upon

various thermal properties, namely thermal conductivity (k_f), density (ρ), specific heat (C_p), viscosity (μ), and the volume concentration of nanoparticles (ϕ). The volume concentration of nanoparticles is a quantitative measure that represents the proportion of the volume occupied by suspended solid nanoparticles to the overall volume of the nanoparticle–fluid mixture. Mathematically, it is expressed as the ratio of the volume of nanoparticles to the total volume of the NF mixture [15]. In order to increase the heat transfer capabilities of the base fluid, it can be replaced with NF [16]. Mixing the base fluid with NPs to enhance the thermal and optical performance of the solar collectors incorporated has been widely reported in the open literature [17]. Some of the widely used NPs by researchers are Cu, CuO, Al, Al_2O_3 , TiO_2 , SiO_2 , and Fe, with Al_2O_3 being the most reported one [18]. A wide range of literature has covered the effect of NFs on the various kinds of solar collectors tabulated in Table 1.

Computational analysis of NF-augmented thermal performance investigation on PTCs was reported in the literature. It was found that NFs are suitable candidates for the efficiency enhancement of PTC. In this regard, Sokhansefat et al. [45] did a numerical study on a three-dimensional SPTC for fully developed turbulent flow using Al_2O_3 /synthetic oil NF. It was concluded that the convective heat transfer coefficient (h) is directly proportional to the nanoparticle concentration. Kaloudis et al. [46] numerically investigated the thermal performance of a SPTC using Al_2O_3 -water NF. A two-phase model for a circular tube under constant wall temperature conditions was taken. Up to 10% improvement in collector efficiency for Al_2O_3 NPs of 4% by mass was reported. In another work, Xiong et al. [47] used Cu/water to access the heat transfer and flow characteristics of PTC. The study revealed that using shear-thinning NF instead of shear-thickening one is more beneficial and helps enhance the system's thermal performance. Nandan et al. [48] modeled the PTC by considering the constant heat-flux condition for the outer surface in both circumferential and longitudinal directions using copper oxide/therminol NF. Nazir et al. [49] used water–boehmite alumina (ALOOH) NF in a semicircular PTC. The highest energy efficacy of the system was reported at $\phi = 4\%$. Hussein et al. [50] numerically investigated the thermo-hydraulic performance of the PTC. Three different kinds of hybrid NFs (Ag-MWCNT, Ag-SWCNT, and Ag-MgO) were applied with a mixing ratio of 50:50 in Syltherm oil 800 base fluid. An increment of 11.5% in thermal efficiency was reported. Karimi et al. [51] used the population balance method to study heat transfer using various nanoparticles. Alnaqi et al. [52] inserted the two twisted tapes in the PTC using MgO-MWCNT/thermal oil hybrid NF to improve the thermal–hydraulic performance. Performance evaluation criterion (PEC) for the thermal system was calculated, and optimum system performance

Table 1 Thermal performance improvement of various solar collectors using NFs

Author(s)/year	Configuration used	Nanofluid used	Operating parameters	Key findings
Otanicar et al. (2010) [19]	Micro-solar-thermal-collector	Carbon nanotubes (CNTs)/H ₂ O, graphite/H ₂ O, silver/H ₂ O	CNT (ϕ)=0.1%, silver (ϕ)=0.25%, graphite (ϕ)=0.1% Flow rate=42 mL h ⁻¹	The overall thermal performance of the system improved by up to 5% when NF was utilized as a carrier for the collector
Lu et al. (2011) [20]	PTC	CuO/H ₂ O	Mass concentration of CuO = 0.8–1.5%	With the implementation of NF, thermal performance increased significantly, and h was enhanced by 30% compared to DI water
Yousefi et al. (2012) [21]	FPC	Al ₂ O ₃ /H ₂ O	Mass concentration = 0.2% and 0.4% Mass flow rate = 1 to 3 lpm	Efficiency went up to 28.3% for 0.2 mass% of Al ₂ O ₃
Yousefi et al. (2012) [22]	FPC	MWCNT/H ₂ O	Mass concentration = 0.2% and 0.4% Mass flow rate = 0.0167 to 0.5 kg s ⁻¹	For 0.2 to 0.4 mass% of MWCNT, a substantial increase in the efficiency of the SFPC was reported
Lenert et al. (2012) [23]	PTC	Carbon-coated absorbing nanoparticles/H ₂ O	-	The efficiency of the thermal system increased by up to 35% using NF
Zadeh et al. (2015) [24]	PTC	Synthetic oil/Al ₂ O ₃	ϕ = 2 to 5% Mass flow rate = 0.9 kg s ⁻¹	At 5% volume concentration of NP, h enhanced up to 11.5%
Kasaean et al. (2015) [25]	PTC	Oil-based NF with CNT	ϕ = 0.2% and 0.3%	A hike of 11% in the efficiency of the PTC was found
Basbous et al. (2016) [26]	PTC	Al ₂ O ₃ /H ₂ O, Cu/H ₂ O, CuO/H ₂ O, Ag/H ₂ O	ϕ = 5% for Al ₂ O ₃ , CuO and Ag	Ag/water performed best among these NFs with an enhancement of about 36% in the h, and the overall heat loss coefficient was decreased by 31%
Bellos et al. (2016) [27]	PTC	A mixture of thermal oil and Al ₂ O ₃	ϕ = 2% Re = 4000 to 25,000	NP-enriched test fluid enhanced the efficiency of the collector by 4.25%
Iranmanesh et al. (2017) [28]	(ETC)	Graphene Nanoplatelets (GNPs)/H ₂ O	Mass concentration of GNPs = 0.025–0.1% Volume flow rate = 0.1, 0.5, and 1.5 lpm	ETC incorporated with GNP/DI water NF showed tremendous thermal performance with a hike of about 90.7% in collector efficiency
Jouybari et al. (2017) [29]	FPC	SiO ₂ /H ₂ O	ϕ = 0.2, 0.4 and 0.6% Volume flow rate = 0.5, 1.0, and 1.5 lpm	The thermal efficacy of the collector was enhanced to 8.1% using SiO ₂ /DI water NF as a flowing media
Colangelo et al. (2017) [30]	FPC	Al ₂ O ₃ /H ₂ O	ϕ = 0 to 3% Flow rate = 0.02 kg s ⁻¹	The thermal efficiency of the nano-incorporated collector improved by 7.54% when Al ₂ O ₃ NPs were mixed with a volume concentration of 3%
Khakrah et al. (2017) [31]	PTC	Al ₂ O ₃ /synthetic oil	ϕ = 0 to 5% Wind speed = 5 to 20 m s ⁻¹	At a 5% volume concentration of Al ₂ O ₃ , the thermal efficacy of the PTC was enhanced by 14.3% for a horizontal reflector

Table 1 (continued)

Author(s)/year	Configuration used	Nanofluid used	Operating parameters	Key findings
Chamkha et al. (2018) [32]	Photovoltaic thermal solar collector	SiO ₂ /H ₂ O	$\phi = 2$ to 5% Re = 500	The thermal performance of the system was maximized at the maximum volume concentration of NPs, with an increment of 7.39% in thermal efficiency
Mercan et al. (2019) [33]	Evacuated tube collector (ETC)	Al ₂ O ₃ /H ₂ O, CuO/H ₂ O	$\phi = 1$ to 5% Mass flow rate = 0.025 to 0.07 kg s ⁻¹	CuO/water showed maximum improvement in h with an enhancement of 6.8%, whereas for Al ₂ O ₃ /water, it was 4.13%
Hong et al. (2021) [34]	PTC	Cu/H ₂ O	$\phi = 0, 1,$ and 2% Re = 10 ⁴ , 10 ⁵ , and 10 ⁶	The increment in the thermal efficiency of about 1.6%, 2.5%, and 1.8% was reported for the NF-augmented PTC for Re = 10 ⁴ , 10 ⁵ , and 10 ⁶ , respectively
Ashour et al. (2022) [35]	FPSC	H ₂ O/CuO, H ₂ O/ZnO	$\phi = 0.05, 0.10$ and 0.15% Mass flow rate = 0.0125 and 0.025 kg s ⁻¹	CuO/water showed the best result between these two NFs, intensifying by about 81.64% in thermal efficiency
Arun et al. (2022) [36]	PTC	TiO ₂ /H ₂ O	$\phi = 0.1$ to 0.5% Mass flow rate = 0.5 to 3 kg/min	The system's overall efficiency was maximized by 34.25% compared to the base fluid
Samiezadeh et al. (2022) [37]	PTC	Cu-Al ₂ O ₃ /oil	$\phi = 0$ to 3% Re = 5 × 10 ³ –5 × 10 ⁵	The h enhanced by 13% at Re = 5 × 10 ⁵ , $\phi_{Cu} = 1%$ with no Al ₂ O ₃ NPs
Khaledi et al. (2023) [38]	Compound parabolic collector (CPC)	SiO ₂ /ethylene glycol (EG)-water	$\phi = 0.5, 1.0$ and 1.5% Volume flow rate = 1 to 2.5 lpm Velocity inlet = 0.1 to 3.5 m s ⁻¹	At $\phi = 1.5%$, the collector's thermal performance maximized 10.43%
Dou et al. (2023) [39]	PTC	Synthetic oil/Cu	$\phi = 1, 3,$ and 5%	The thermal and exergy efficiency was enhanced by 7.99% and 8% for a volume concentration of 0.05% Cu NPs
Tavakoli et al. (2023) [40]	PTC	Al ₂ O ₃ -MWCNT/H ₂ O	$\phi = 0$ to 3% Re = 5 × 10 ³ –3.5 × 10 ⁴	At $\phi = 0%$ and Re = 2 × 10 ⁴ , the collector efficiency enhanced by 1.62%
Ekiciler et al. (2023) [41]	PTC	ZnO/EG-H ₂ O	$\phi = 1$ to 4% Volume flow rate = 20 to 40 L per hour	Nusselt number (Nu) increased by almost 100% at $\phi = 4%$
Esmaceli et al. (2023) [42]	PTC	Al ₂ O ₃ -Cu/H ₂ O	Al ₂ O ₃ (ϕ) = 3%, Cu (ϕ) = 1% Re = 5150 to 9364	With the combined effect of turbulator and NF, the h increased by 57.3%
Pazarlioğlu et al. (2023) [43]	PTC	TiO ₂ -Syltherm800, Al ₂ O ₃ -Syltherm800, TiO ₂ -Al ₂ O ₃ /Syltherm800	$\phi = 0.5$ to 2% Re = 10 ⁴ –3 × 10 ⁴	The use of Al ₂ O ₃ (1.5%)-TiO ₂ (0.5%)/Syltherm800 NF showed an efficiency improvement of 16%, whereas the performance evaluation criterion (PEC) increased by 37%

was reported at $\phi = 2\%$. Ekiciler et al. [53] utilized a combination of nanoparticles to investigate the thermal performance of PTC. Among all other NFs, Ag–MgO/Syltherm 800 at a volume fraction of 4% showed maximum improvement in the thermal efficacy of the system.

The literature review clarifies that significant research was carried out on the experimental and numerical studies of SPTC. However, studies on NF-augmented trough collectors are scarce. Moreover, in most studies, constant heat flux on the periphery of the receiver tube was considered to model SPTC. In actuality, the bottom half of the periphery of the receiver tube deals with the beam radiation, whereas the upper half of the periphery deals with global radiation. The range of Re reported in the literature mainly pertains to the laminar region. Literature pertaining to the high turbulent regime Reynolds number (Re) $> 3 \times 10^4$ is scarce to the best of the author's knowledge. Also, the literature review provides convincing proof that Fe_2O_3 nanoparticles have been underutilized in solar applications despite their superior thermal properties compared to several other metallic oxide nanoparticles. In support of this standpoint, the experimental assessment of the cooling capacity of NFs incorporating TiO_2 and Fe_2O_3 was conducted by Babar et al. [54] to cool electronic components. The comparative analysis of the results revealed that NFs formulated with Fe_2O_3 had enhanced performance compared to NFs formulated with TiO_2 . Also, from an economic standpoint, Fe_2O_3 NPs are considered one of the most cost-effective options among other types of nanoparticles. This is evident from the price comparison of different nanoparticle types per 100 g, as illustrated in Fig. 1. Therefore, based on the aforementioned research gaps, an attempt has been made to cover all these areas. The key objectives are listed below.

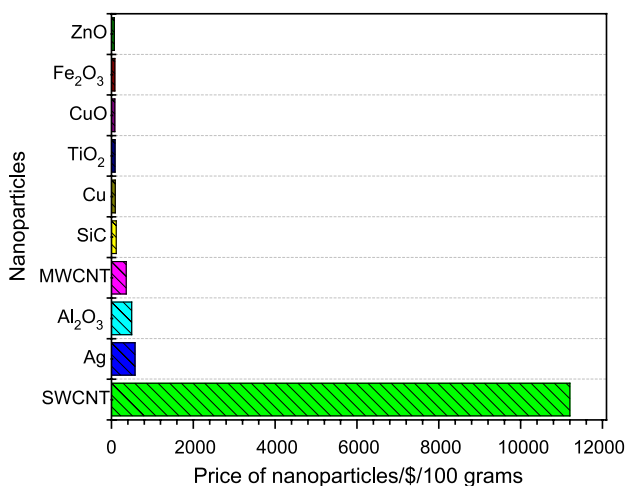


Fig. 1 Price of different nanoparticles (\$/100 g) [57]

- CFD-based numerical investigation of Fe_2O_3 - H_2O NF-augmented solar parabolic trough collector for fully developed turbulent flow.
- Despite the fact that ferric oxide (Fe_2O_3) has the potential to facilitate efficient heat transport, its volume concentration (ϕ) is chosen between 0.5 and 1.0%. The rationale for this phenomenon is attributed to the limited duration of suspension stability exhibited by Fe_2O_3 [55].
- To analyze the flow behavior characteristics of heat transfer fluid (HTF) under a high flow regime. For this, the range of Re is taken as 3×10^4 to 2.6×10^5 . The key reason behind choosing this range is the enhanced heat transfer rate in the high turbulent flow regime. As a conclusive remark, the observed disparity in thermal boundary layer growth at various axial locations along the receiver tube between turbulent and laminar flow is around tenfold [56].

The first section of this paper discusses the background and the working principle of PTC. The following section mentions problem-statement and basic governing equations related to solar collectors. It is followed by the boundary conditions applied on SPTC. Also, the grid sensitivity test and validation of the numerical model are presented. After that, the numerical findings pertaining to flow parameters are presented in the results and discussion part. In addition, the contours of velocity, temperature, and turbulent kinetic energy are also mentioned. For working engineers, easy-to-use simplified correlations have been presented.

Solar parabolic trough collector (SPTC)

A parabolic trough collector is shown in Fig. 2, consisting of a straight receiver tube and a parabolic reflecting surface usually made of a skinny silver layer. The straight receiver tube is placed along the focal axis of the parabolic reflecting surface. Due to manufacturing constraints, the receiver tube length is usually kept below 5 m. When the reflected solar radiation concentrates onto the tube, the circulating fluid gets heated by absorbing the solar energy. Based on the application, the straight receiver comes with an evacuated or non-evacuated tube. For high-temperature applications (above $300^\circ C$), evacuated tube is suggested because it has a high vacuum between the glass cover and pipe, which helps to reduce the thermal losses. For low-temperature applications, a non-evacuated tube is used where the heat losses are not a big concern.

Problem statement

The schematic diagram of the receiver tube of the PTC is illustrated in Fig. 3. The tube length is 2000 mm, and the inner and outer diameters of the tube are 60 mm and 64 mm. The

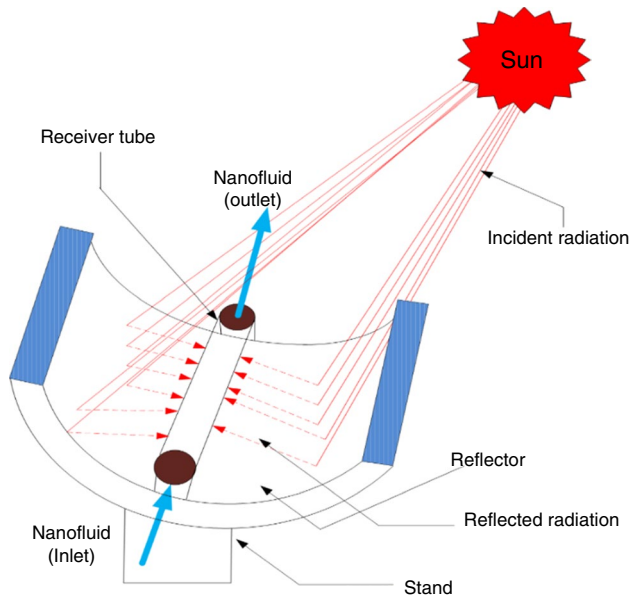


Fig. 2 Solar parabolic trough collector

diameter and range of ϕ of ferric oxide (Fe_2O_3) NPs are 40 nm and 0.5% to 1%, respectively. The fragmented heat-flux condition is applied by dividing the receiver tube into two parts: the upper and bottom half periphery. Accordingly, solar heat

flux is applied on the surface of the absorber tube, and the fluid flow characteristics are analyzed for PTC incorporated with Fe_2O_3 /water NF at six different volume concentrations (ϕ) ranging between 0.5 and 1.0%.

Governing equations

The governing equations for the case of the steady-state fully developed turbulent flow for an incompressible fluid in cylindrical coordinates can be summarized as follows [58]:

Continuity equation:

$$\frac{1}{r} \frac{\partial}{\partial \theta}(\rho u) + \frac{1}{r} \frac{\partial}{\partial r}(\rho r v) + \frac{\partial}{\partial Z}(\rho w) = 0 \tag{1}$$

or

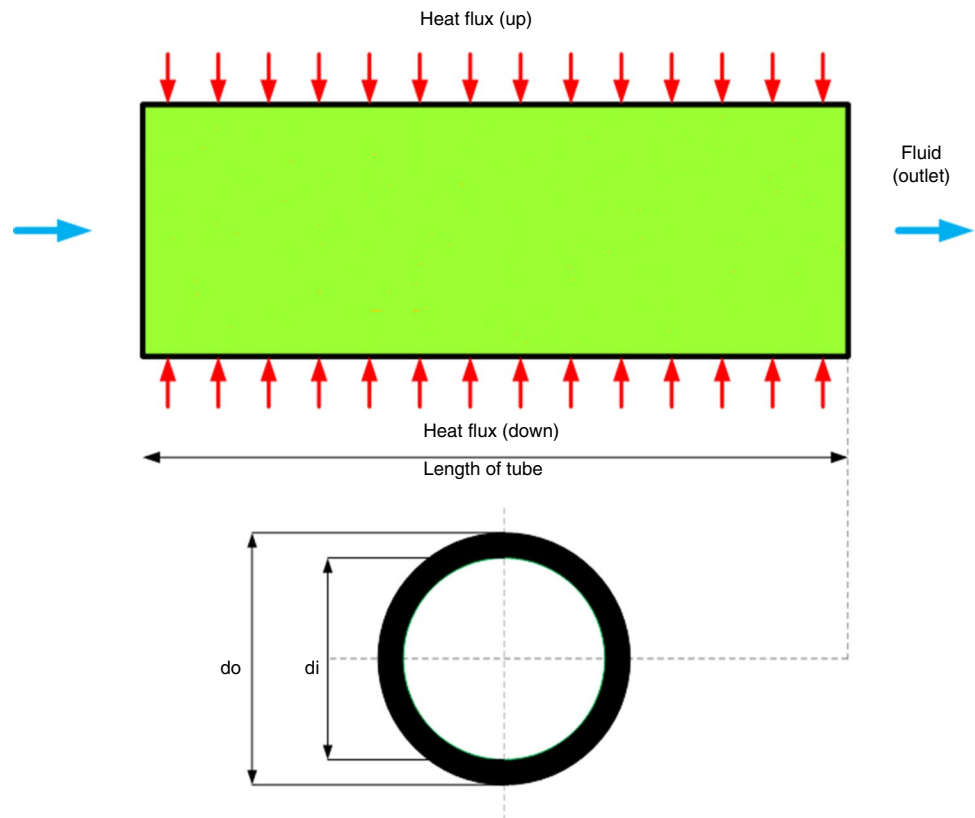
$$\nabla \cdot (\rho V) = 0 \tag{2}$$

where $V = (V_r, V_\theta, V_z)$ is defined as the velocity field for different spatial coordinates.

Momentum equations:

$$\nabla \cdot (\rho V V_i) = \frac{-\partial p}{\partial x_i} + \nabla \cdot (\mu \Delta V_i) + S_i \tag{3}$$

Fig. 3 Schematic diagram of the solar receiver tube



where $X_i = R, \theta, Z$ for different cylindrical coordinates. The viscous term associated with the above equation for different types of spatial coordinates can be given below;

For radial direction ($i = 1$);

$$S_1 = \rho V_\theta \frac{V_\theta}{r} - \mu \left[\frac{V_R}{r} + \left(\frac{2}{r^2} \right) \frac{\partial V_\theta}{\partial \theta} \right] \tag{4}$$

For tangential direction ($i = 2$);

$$S_2 = \mu \left[\left(\frac{2}{r^2} \right) \frac{\partial V_R}{\partial \theta} - \frac{V_\theta}{r^2} \right] - \rho V_R \frac{V_\theta}{r} \tag{5}$$

For axial direction ($i = 3$);

$$S_3 = 0 \tag{6}$$

Energy equation:

$$\nabla \cdot (\rho V C_p T) = \nabla \cdot (k_f \nabla T) \tag{7}$$

where $\rho, \mu, C_p,$ and k_f are the fluid density, dynamic viscosity, specific heat, and thermal conductivity of the circulating fluid, respectively.

$k - \epsilon RNG$ turbulence model is employed to capture the flow behavior. The governing equations for the turbulence model are given in Eqs. (8) and (9), respectively [59].

$$\nabla \cdot (\rho V k) = \nabla \cdot \left[\left(\mu + \frac{\mu_t}{\sigma_k} \right) \nabla k \right] + G_k - \rho \epsilon \tag{8}$$

$$\nabla \cdot (\rho V \epsilon) = \nabla \cdot \left[\left(\mu + \frac{\mu_t}{\sigma_\epsilon} \right) \nabla \epsilon \right] + C_{1\epsilon} \left(\frac{\epsilon}{k} \right) G_k - C_{2\epsilon}^* \times \rho \left(\frac{\epsilon^2}{k} \right) \tag{9}$$

where ϵ and k is the dissipation rate and turbulent kinetic energy, respectively. Turbulent kinetic energy generation caused by mean velocity gradients is represented by G_k . σ_ϵ and σ_k are the Prandtl number for turbulent flow for ϵ and k , respectively. Constants are shown by $C_{1\epsilon}$ and $C_{2\epsilon}$ and eddy or turbulent viscosity is written as μ_t . The empirical constants associated with the $k - \epsilon RNG$ turbulent model are listed below [60];

$$\mu_t = \rho C_\mu (k^2/\epsilon), \quad C_\mu = 0.0845, \quad C_{1\epsilon} = 1.42 \tag{10}$$

$$C_{2\epsilon}^* = C_{2\epsilon} + \frac{C_\mu \eta^3 (1 - \eta/\eta_0)}{1 + \beta \eta^3}, \quad C_{2\epsilon} = 1.68, \quad \eta_0 = 4.38 \tag{11}$$

$$\eta = \frac{k}{\epsilon} (2E_{ij}E_{ij})^{1/2}, \quad \sigma_k = 1, \quad \sigma_\epsilon = 1.3 \tag{12}$$

$$G_k = 2\mu_t E_{ij}E_{ij}, \quad E_{ij} = \frac{1}{2} \left(\frac{\partial u_i}{\partial x_j} + \frac{\partial u_j}{\partial x_i} \right), \quad \beta = 0.012 \tag{13}$$

Thermophysical properties of nanofluid

For the current numerical study, co-relations used for the calculation of density and specific heat of NF are given below [61]:

$$\rho_{nf} = (1 - \phi)\rho_{bf} + (\phi\rho_{nf}) \tag{14}$$

$$(\rho C_p)_{nf} = (1 - \phi)(\rho C_p)_{bf} + \phi(\rho C_p)_{nf} \tag{15}$$

The density (ρ_{nf}) and specific heat ($C_{p,nf}$) of NF are assumed to be a linear function of the volume concentration of NPs. The other two essential thermal properties of NF, i.e., thermal conductivity (k_{eff}) and dynamic viscosity (μ_{eff}), depend not only upon volume concentration (ϕ) but also strongly dependent on mixture combination, size of the nanoparticle, surfactant mixed, slip mechanism, etc. For the current study, Fe_2O_3 (40 nm) NP is chosen. The material properties of the H_2O and Fe_2O_3 NPs are mentioned in Table 2.

The expression for the thermal conductivity employed by Xuan et al. [63] is given as:

$$\frac{k_{eff}}{k_{bf}} = \left[\frac{(k_{np} + 2 \times k_{bf}) - 2 \times \phi(k_{bf} - k_{np})}{(k_{np} + 2 \times k_{bf}) + \phi(k_{bf} - k_{np})} \right] + \frac{\rho_{nf} \times \phi \times C_{p,bf}}{2 \times k_{bf}} \times \left(\frac{2 \times K_b \times T_{avg}}{3 \times \pi \times d_p \times \mu_f} \right)^{0.5} \tag{16}$$

where d_p is the nanoparticle diameter, and K_b is the Boltzmann constant. The effect of Brownian motion and the aggregation of the NPs is considered. Further, it is considered that the thermal conductivity of NF is a function of the size of the NPs, the volume fraction of NPs, the thermal conductivity of NPs (k_{np}), the average temperature of the mixture, and various other thermal properties of base fluid, including viscosity, specific heat capacity, and thermal conductivity.

Based on the literature, it is found that in most of the numerical studies, the effect of viscosity is shown through either the Einstein model [64] or the Brinkman model [65]. All these models have considered only the effect of the addition of volume concentration of NPs. In the present

Table 2 Thermophysical properties of the base fluid and nanoparticle [62]

Properties	Base fluid (H_2O)	NPs (Fe_2O_3)
$\rho / \text{kg m}^{-3}$	998.2	5250
$C_p / \text{J kg}^{-1} \text{K}^{-1}$	4182	650
$k_f / \text{W m}^{-1} \text{K}^{-1}$	0.613	20
$\mu / \text{Pa s}$	0.001003	-

study, the Corcione model [66] for viscosity is chosen in which it is shown that effective NF viscosity depends upon the molecular diameter of base fluid and nanoparticles, i.e., ($d_{\text{base fluid}}$) and (d_{np}), respectively, and is given as:

$$\frac{\mu_{\text{eff}}}{\mu_{\text{bf}}} = \frac{1}{1 - 34.87 \times \left(\frac{d_{\text{np}}}{d_{\text{bf}}}\right)^{-0.3} \times \phi^{1.03}} \quad (17)$$

where d_{bf} can be calculated by knowing the molecular mass of the base fluid (M) and is given as:

$$d_{\text{bf}} = 0.1 \left[\frac{6 \times M}{N \times \pi \times \rho_{\text{bf},0}} \right]^{1/3} \quad (18)$$

where N is the Avogadro number (6.022×10^{23}), and the density of the fluid is calculated at 293K.

Boundary conditions

Fragmented heat flux is applied over the periphery of the receiver tube by applying beam radiation at the bottom half of the tube, whereas the top half periphery receives the global radiation. The following mentioned boundary conditions are applied to the receiver tube of the parabolic trough collector:

- Inlet boundary condition: At the inlet of the receiver tube, a uniform velocity corresponding to a particular Reynolds number is taken. The fluid temperature at the inlet is taken as 300 K.

$$u = U_{\text{inlet}}, T_{\text{fluid}} = T_{\text{inlet}} = 300 \text{ K, at } L = 0$$

- Wall boundary condition: No-slip conditions are applied for the wall-fluid interface.

$$u = 0, \text{ at } r = d/2$$

- The outer periphery of the receiver tube is split into two parts.

$$(a) q''_{\text{top}} = I_g$$

$$(b) q''_{\text{down}} = I_b \times C_R$$

Here, C_R = concentration ratio = A_p/A_r , I_g = global radiation (800 W m^{-2}), I_b = beam radiation (600 W m^{-2}), A_p = aperture area of trough collector and A_r = absorber tube area.

- Outlet boundary condition: a zero-pressure gradient is employed across the outer boundary at the receiver tube outlet.

Dimensionless parameters

Nusselt number (Nu) is assessed to study the thermal performance of the PTC. The Nu is used to contrast the convective and conductive heat transfer mechanisms and can be defined as:

$$\text{Nu} = \frac{h \times L_c}{k_f} \quad (19)$$

where L_c stands for the characteristic length of the absorber tube of PTC, k_f is the thermal conductivity of the HTF, and h is the convection heat transfer coefficient. It is defined as below:

$$h = \frac{q}{(T_{\text{wall}} - T_f)} \quad (20)$$

where T_{wall} is the average surface temperature of the receiver tube of PTC.

Reynolds number (Re) is given as:

$$\text{Re} = \frac{U \times L_c}{\rho_f} \quad (21)$$

The dimensionless friction factor is a crucial metric to analyze the pressure drop via the receiver tube. It illustrates how operational factors affect pumping efficiency and is given as:

$$f = \frac{2 \times \Delta P \times L_c}{L \times \rho \times U_{\text{in}}^2} \quad (22)$$

where ΔP , L , and U_{in} stand for the pressure drop associated with the receiver tube, the length of the receiver tube, and the inlet velocity of the HTF successively.

The balance between thermal improvement and the requisite source of pumping power must be taken into account when assessing the efficacy of the nanofluid-augmented PTCs. For this, a non-dimensional number is suggested called the Performance evaluation criterion (PEC) [67]. The need for PEC for any thermal system in which nanofluid is used is vital to assess the overall efficacy of the system. In this regard, PEC is evaluated according to Eq. (23), which tells whether the thermal system employed with nanofluid is feasible. Generally, greater than unity is taken as a benchmark for this purpose.

$$\text{PEC} = \frac{\frac{\text{Nu}}{\text{Nu}_0}}{\left[\frac{f}{f_0}\right]^{1/3}} \quad (23)$$

where Nu_0 and f_0 stand for the Nusselt number and friction factor of the base fluid, respectively.

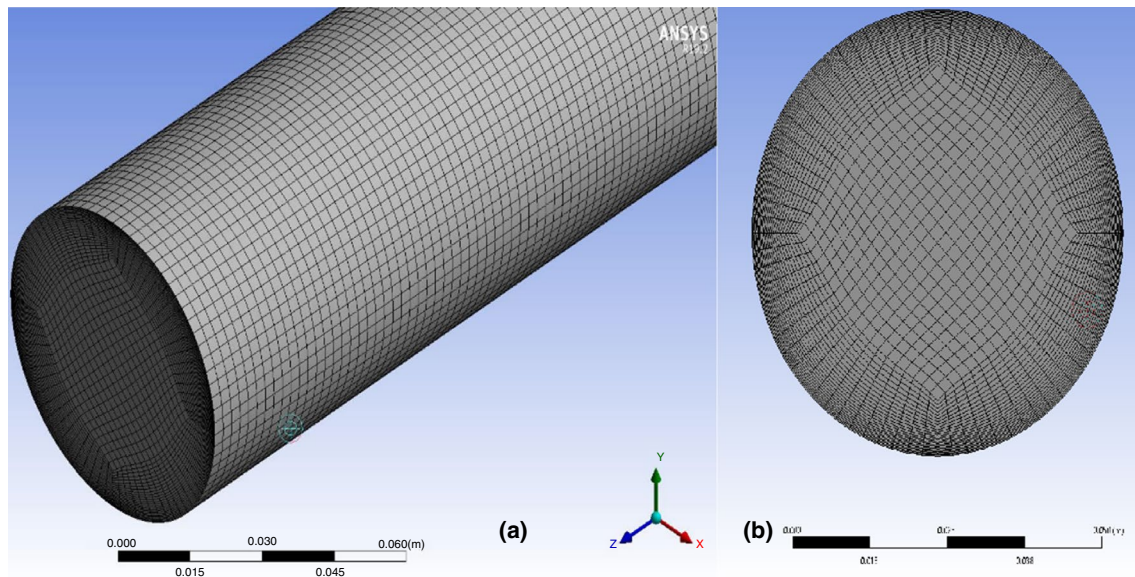


Fig. 4 Grid generation for the computational domain: **a** outer periphery of receiver tube, **b** inlet and outlet section of the receiver tube

If the $PEC > 1$: this means that heat transfer capabilities are more than the increased pressure drop, and hence the system is feasible.

If the $PEC \leq 1$: this implies that heat transfer enhancement is lower than or equal to the pumping power, which negates the need to use the NF in place of any traditional base fluid.

Numerical methodology

A finite volume-based algorithm is employed in the current study to model nanofluid flows in the system using a single-phase model. A semi-implicit approach for pressure-linked equations consistent (SIMPLEC) algorithm is used to solve the pressure–velocity coupled equations. Moreover, the second-order upwind technique is used to solve the diffusion and convection terms included in the governing equations. The discretized form of the energy equation is then solved after the continuity and momentum equations are solved. The algebraic equations are then solved using the Jacobi conjugate gradient technique. While examining the convergence characteristics of continuity and momentum equations, the residual values are assumed to be 10^{-4} . However, the maximum residual for the energy equation is set at 10^{-6} .

Grid generation and mesh sensitivity test

A three-dimensional structured grid is employed to solve the present numerical model. The simulated geometry of

the receiver tube of PTC is made in the design modular of ANSYS R19.2 commercial solver. At the inlet and outlet of the receiver tube, a combination of tetrahedral and hexahedral meshing is considered, whereas hexahedral meshing with eight nodes is considered for the rest of the section. Uniform-sized cells are considered along the length of the tube due to constant velocity and temperature gradients in the z -direction. Figure 4 shows the grid generation for the computational domain. Near the pipe wall, layers have been inflated. To keep the computation time and cost in control, finer grids only near the boundary walls have been considered. It also helps to capture the gradients given at the wall surfaces efficiently and provides accurate results.

A mesh sensitivity test is carried out to ensure the grid independency. As shown in Fig. 5. Five cases with total cell counts of 513,882, 756,154, 1,432,722, 1,804,442, and 2,198,430 are taken into consideration. The surface heat transfer coefficient (h_{sur}) is determined in each of the five cases, and the results are compared to the values obtained in case 5 with 2,198,430 cells. For the last two cells, values obtained for h_{sur} are nearly constant, with a difference of 0.185%. Hence, a grid size of 1,804,442 cells is considered.

Validation

Validation of the present numerical model is illustrated in Figs. 6 and 7. Numerical values of Nusselt number, Nu and friction factor, f are calculated and compared with the available results given by Ghasemi et al. [68] and from the Petukhov correlations for fully developed turbulent flow [69] as given in Eqs. (24) and (25). Results show excellent

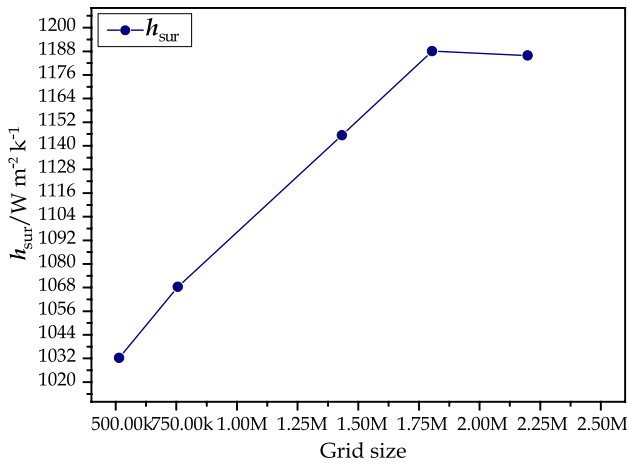


Fig. 5 Mesh sensitivity test for surface heat transfer coefficient

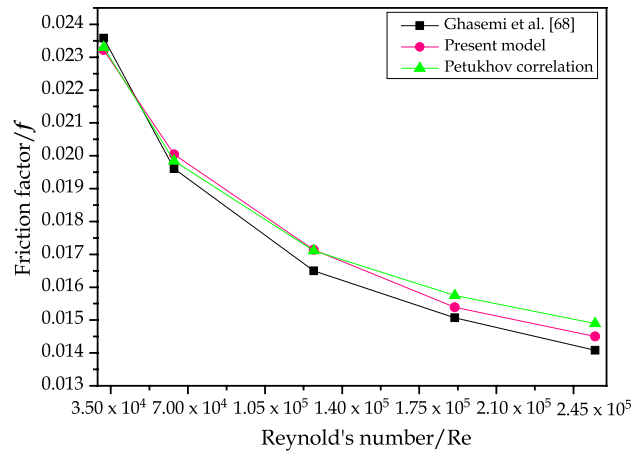


Fig. 7 Validation of friction factor with Ghasemi et al. [68] and Petukhov correlation

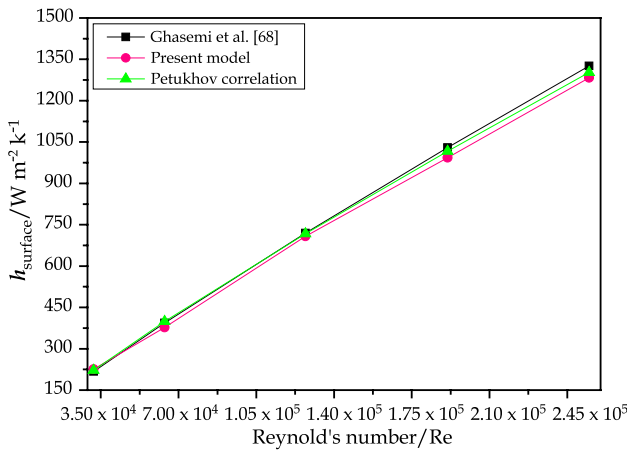


Fig. 6 Validation of surface heat transfer coefficient with Ghasemi et al. [68] and Petukhov correlation

agreement with earlier results having a variation of not more than 6.0%.

Petukhov correlation [69] for Nu and f are mentioned below:

$$Nu = \frac{\left(\frac{f}{8}\right) Re \cdot Pr}{1.07 + 12.7 \left(\frac{f}{8}\right)^{0.5} (Pr^{2/3} - 1)} \quad (24)$$

for $10^4 \leq Re \leq 5 \times 10^6, 0.5 \leq Pr \leq 2000$

$$f = (0.79 \ln(Re) - 1)^{-2} \quad (25)$$

Results and discussion

Variation of thermal properties of nanofluids

Based on the correlations presented from Eqs. (15) to (19), the thermal properties variation of NFs with the volume concentration (ϕ) of NPs ranging between 0.5 to 1.5% is depicted in Fig. 8. In corresponds to Fig. 8a, the density of NF increased linearly with ϕ . At $\phi=0.5\%$, the density of the mixture is increased by 1.94% compared to the base fluid. For a change in ϕ from 0.5 to 1.5%, the density of the NF mixture increased by 6.38%. In Fig. 8b, the specific heat of the NF mixture decreases with the concentration of nanoparticles. It is found that the C_p of the NF is decreased by 2.547% compared to base fluid with the suspension of a tiny amount of NPs at $\phi=0.5\%$. The C_p of the NF is found to be 4003.825 at $\phi=1\%$. Further, it decreased by 4.18% when the volume concentration of the NPs varied from $\phi=0.5\%$ to 1.5%. A crucial factor in improving heat transport is thermal conductivity (k_f), and its variation with ϕ is depicted in Fig. 8c. At $\phi=0.5\%$, the improvement in k_f was 3.57%, whereas, for $\phi=1.0\%$, the percentage enhancement in the k_f was found to be 5.567%. The maximum enhancement in k_f is recorded as 6.423% at $\phi=1.5\%$, which proves that the NFs have remarkably high k_f and can be used as a HTF in various applications. Viscosity is crucial because it resists fluid mobility. The base fluid becomes more viscous when solid particles are introduced, because of which pressure drop increases. For a rise in the concentration of NPs from 0.5 to 1.5%, an increase in the viscosity of the test fluid by 2.56% is obtained, as shown in Fig. 8d.

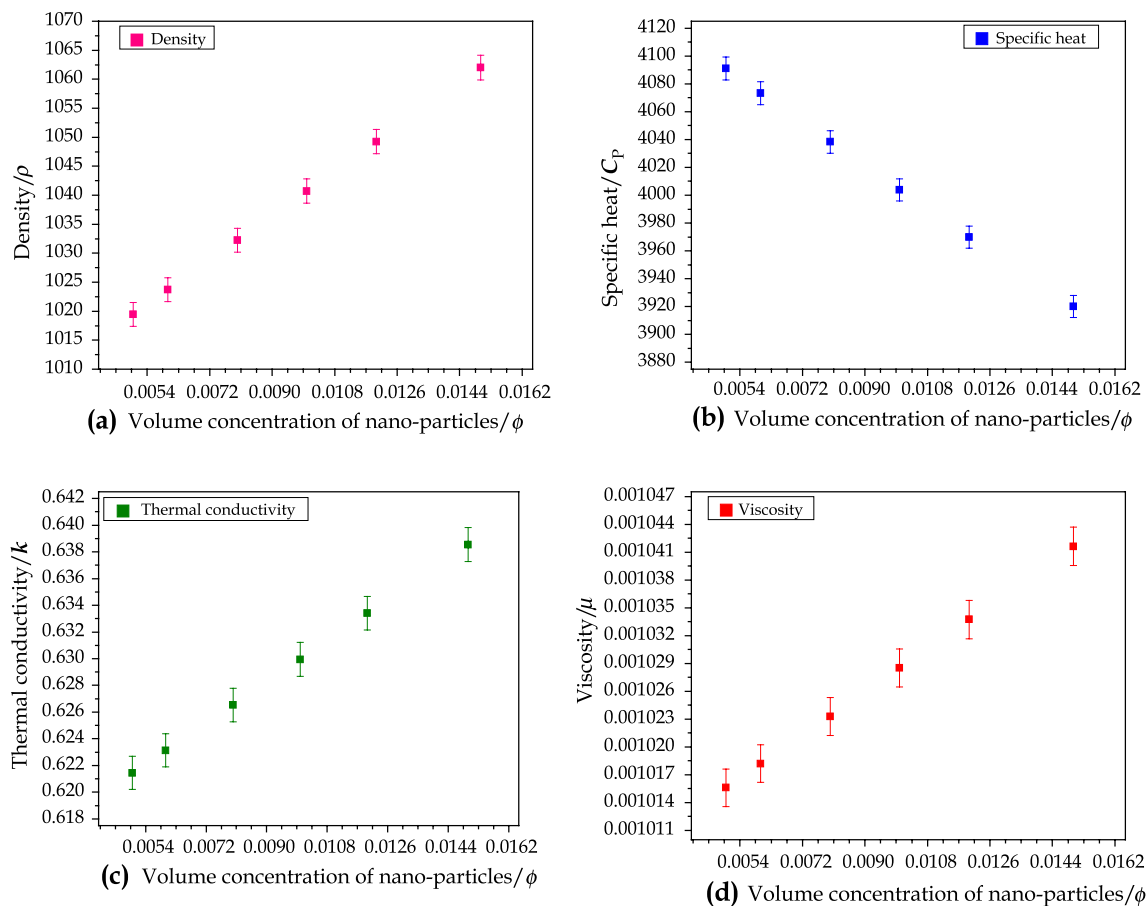


Fig. 8 Variation of thermal properties for Fe₂O₃/water NF with volume concentration (ϕ); (a) density, (b) specific heat, (c) thermal conductivity, (d) viscosity

Contours of velocity, temperature, and thermal kinetic energy

The contours of streamwise velocity distribution at the receiver tube outlet at $\phi = 1\%$ of Fe₂O₃ NPs at five different Re values are depicted in Fig. 9. As shown in Fig. 9 (a–e) while moving from the center of the receiver tube to the pipe wall; the velocity decreased with the maximum at the center of the tube and zero at the pipe wall. In addition, velocity increases with the increase in the Re value, which is evident as Re is directly proportional to velocity.

The temperature distribution for the receiver tube at $\phi = 1\%$ and different Re are shown in Fig. 10a–e. Due to the fragmented heat-flux heat condition at the periphery of the receiver tube, non-uniformity in the temperature distribution can be seen. Since the solar insolation, after reflecting from the polished parabolic reflector, concentrates on the bottom periphery of the receiver, the temperature around the bottom half periphery of the receiver tube is more than the upper half periphery. In addition,

the temperature of the working fluid is reduced with the increase in the Re. This is due to the increase in the mass flow rate, because of which the time to exchange heat between the fluid and the surface of the receiver tube is decreased. Furthermore, uniformity in the contours can be seen with the increase in Re, which means the temperature distribution of the absorber tube is becoming uniform and extending through wider regions.

The contours of turbulent kinetic energy (TKE) at the outlet of the receiver tube with increasing Re are presented in Fig. 11a–e. It represents the mean kinetic energy per unit mass associated with the eddies current formed in a turbulent flow. Physically, it can be expressed as the computed root-mean-square (RMS) velocity irregularities. For a constant volume concentration of NPs at $\phi = 1.0\%$, the TKE is found to be increasing in nature with the increase in mass flow rate. As the mass flow rate increases, the outer boundary regions of the contours get thicker, which shows that the intensity of the turbulence is increasing.

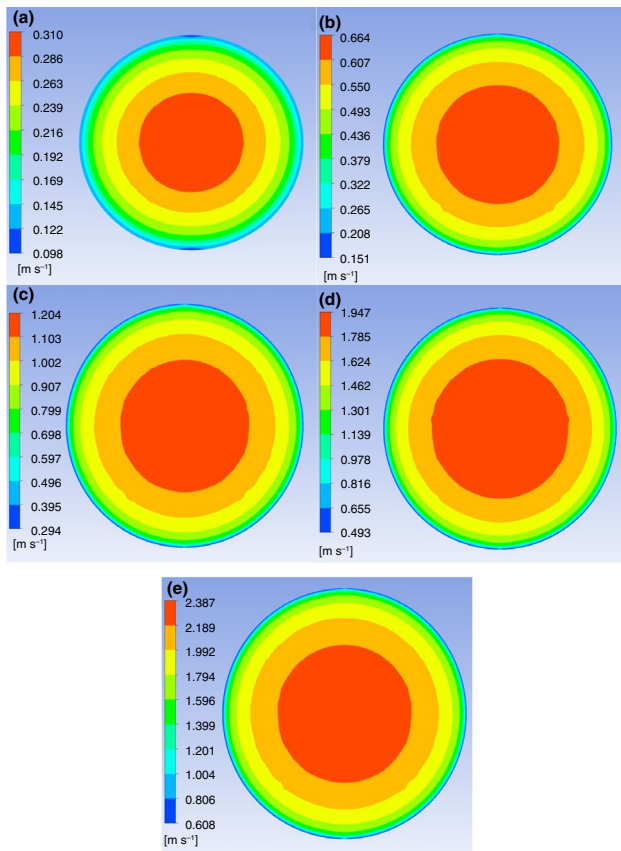


Fig. 9 Velocity contours of receiver tube at the outlet for different Re and at $\phi=1\%$; **(a)** $Re \approx 3 \times 10^4$, **(b)** $Re \approx 6 \times 10^4$, **(c)** $Re \approx 1.2 \times 10^5$, **(d)** $Re \approx 2 \times 10^5$, **(e)** $Re \approx 2.6 \times 10^5$

Flow parameters variation with the Re and volume concentration of NPs (ϕ)

In Fig. 12, the variation of surface heat transfer coefficient (h_{sur}) with the Re for both base fluid and NF at six different volume concentrations of NPs ranging between 0.5 to 1% is depicted. The presented graph shows that the h_{sur} increases with the increase in the Re. With the increase in Re, the formation of eddies and vortices enables thermal energy transfer between the fluid with higher temperatures and the surface with lower temperatures. The continuous mixing process promotes the displacement of stagnant fluid at the surface by introducing fresh fluid, improving the heat transfer rate. Moreover, with the increased fluid velocity, the boundary layer experiences a reduction in its thickness due to the turbulent and disorderly motion. This reduction in thickness leads to a decrease in heat transfer resistance, facilitating an augmented heat transfer across the boundary layer. Besides, with the increase in the volume concentration of NPs (ϕ), the h_{sur} is increasing. Critical examination of the graph signifies that the relative increment in the h_{sur} , at the mass flow rate of 1.5 kg

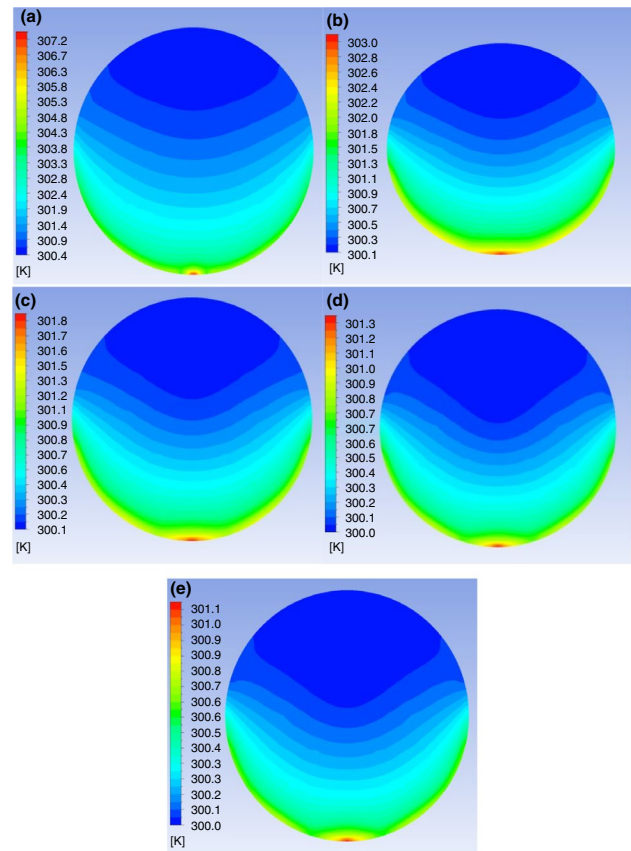


Fig. 10 Temperature contours of receiver tube at the outlet for different Re and at $\phi=1\%$; **(a)** $Re \approx 3 \times 10^4$, **(b)** $Re \approx 6 \times 10^4$, **(c)** $Re \approx 1.2 \times 10^5$, **(d)** $Re \approx 2 \times 10^5$, **(e)** $Re \approx 2.6 \times 10^5$

s^{-1} , is 49.21% compared to base fluid at $\phi=0.5\%$, whereas at $\phi=1\%$, the relative increment in h_{sur} is nearly 57.97%. This enhancement in the h_{sur} is due to the suspended NPs, which possess very high thermal conductivity compared to the water. In addition, in conventional base fluids like water, the existence of a boundary layer may have an undesirable effect on heat transfer efficiency. However, the presence of nanoparticles can potentially impede the establishment of this layer due to their capacity to agitate and homogenize the fluid. Consequently, a reduction in resistance to heat transmission occurs, resulting in an improvement in the heat transfer rate.

The variation of the Nusselt number (Nu) with the increasing Re for both base fluid and NF at six different volume concentrations of NPs ranging from 0.5 to 1.0% is depicted in Fig. 13. It is found that for $Re \approx 6 \times 10^4$ and at $\phi=0.5\%$, the relative increment in the Nu is 50.13%, whereas at $\phi=1.0\%$, it went up to 59.09%. For $Re \approx 2 \times 10^5$ and $\phi=0.5\%$, the relative increment in the Nu is 42.87%. With the increase in ϕ , the Nu is increasing, and a maximum relative increment of 51.11% is found at the same Re and $\phi=1.0\%$.

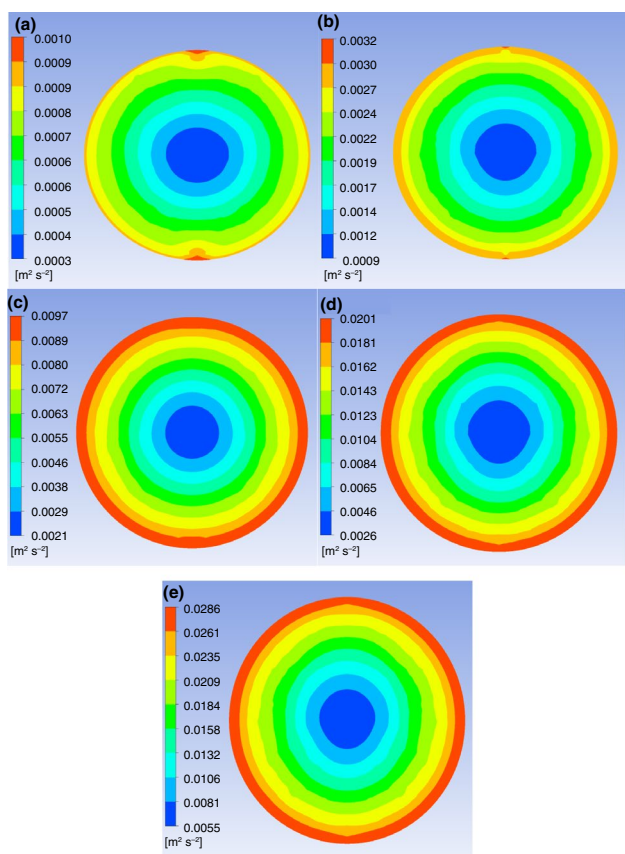


Fig. 11 Turbulent kinetic energy contours of receiver tube at the outlet for different Re and at $\phi = 1\%$; **a** $Re \approx 3 \times 10^4$, **b** $Re \approx 6 \times 10^4$, **c** $Re \approx 1.2 \times 10^5$, **d** $Re \approx 2 \times 10^5$, **e** $Re \approx 2.6 \times 10^5$

Figure 14 shows the variation of relative Nusselt number with Re at six different volume concentrations of NPs. The graph depicts the relative enhancement in Nu by replacing the base fluid with NF. The relative Nu increases with the addition of NPs. The nature of the graph rises until $Re \approx 6 \times 10^4$; after that, it decreases. Furthermore, the percentage increment in the relative Nu is 4.64% for a mass flow rate of 1.5 kg s^{-1} and $\phi = 0.5\text{--}0.6\%$. The percentage increment is reduced to 2.67% at the same mass flow rate and $\phi = 0.9\text{--}1.0\%$. A similar trend is found at $Re \approx 2.6 \times 10^5$, where the percentage increment in the Relative Nu is found to be a maximum of 3.47% at $\phi = 0.5\text{--}0.6\%$, and then it kept on decreasing to a value of 2.04% at $\phi = 0.9\text{--}1.0\%$.

In Fig. 15, the variation of friction factor (f) with the increasing Re for base fluid and NF at six different volume concentrations of NPs ranging from 0.5 to 1.0% is depicted. An inverse relationship between Re and friction factor led to a decreased friction factor with increased fluid inlet velocity. Furthermore, a significant rise in the friction factor can be observed with the rise in nanoparticle concentration. Rise in the density of the whole mixture and increased viscosity is the cause behind this phenomenon. The relative increment

in the friction factor compared to the base fluid is maximum when the mass flow rate is minimum. At this point, the increment is about 30.30% for $\phi = 0.5\%$, whereas for $\phi = 1.0\%$, the friction factor increases to 30.67%. The percentage increment in the friction factor with adding NPs is also examined. It is found that the percentage increment is minimal. For $\phi = 0.9$ and 1.0%, a rise in the friction factor of 0.12% is obtained.

Figure 16 depicts the variation of the relative friction factor with Re at six different volume concentrations of NPs. The suspension of NPs results in increased viscosity, which further assists friction losses to occur predominantly. Investigation reveals that the relative friction factor decreases continuously until $Re \approx 2 \times 10^5$; thereafter, it increases further. The increment in the f is 20.83% at $\phi = 0.5\%$. It continued increasing with ϕ and reached a maximum of 21.51% compared to the base fluid for $\phi = 1.0\%$.

The variation of performance evaluation criterion (PEC) with Re for concentration (ϕ) ranging between 0.5 and 1.0% is depicted in Fig. 17. At any particular mass flow rate, the PEC is found to be more than unity. In addition, it kept on increasing with the increasing ϕ . Initially, at a low mass flow rate, the overall enhancement in PEC is 18.84% when the ϕ changes from 0.5% to 1.0%. At $Re \approx 6 \times 10^4$, a maximum PEC of 2.206 is obtained for $\phi = 1.0\%$; after that, it decreased successively with the increase in mass flow rate of HTF. At $Re \approx 2.6 \times 10^5$, the PEC is assessed, and an increment of 15.42% is obtained with an increase in ϕ from 0.5 to 1.0%.

Correlation for h_{sur} , Nu_{sur} , f and correlation matrix

A set of correlations are developed for the surface heat transfer coefficient (h_{sur}), surface Nusselt number (Nu_{sur}), and friction factor (f), respectively, to maximize the utilization of the obtained data. Such simplified easy-to-use correlations come handy to working engineers. It also helps to quantify the dependency among the variables. Their dependency on Re and volume concentration of NPs (ϕ) are created using regression analysis. Various indices and constants are computed using user-defined code based on partial least square regression methodology. A correlation matrix is also presented in Table 3, clarifying the variables' dependency. Except for the friction factor (f), all other properties have a positive attitude, whereas f has a negative tendency toward the variables.

Correlation for surface heat transfer coefficient (h_{sur})

The correlation for the surface heat transfer coefficient is given in terms of Re and ϕ in Eq. (26). It is valid for $3 \times 10^4 \leq Re \leq 2.6 \times 10^5$ and $0.5 \leq \phi \leq 1.0$. The developed

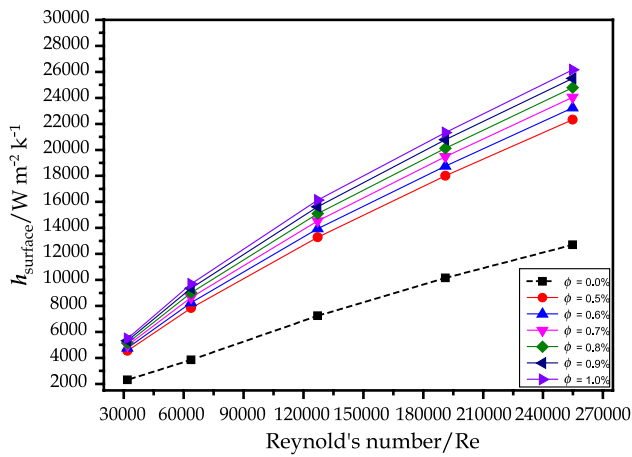


Fig. 12 Variation of surface heat transfer coefficient with Re and addition of volume concentration of NPs

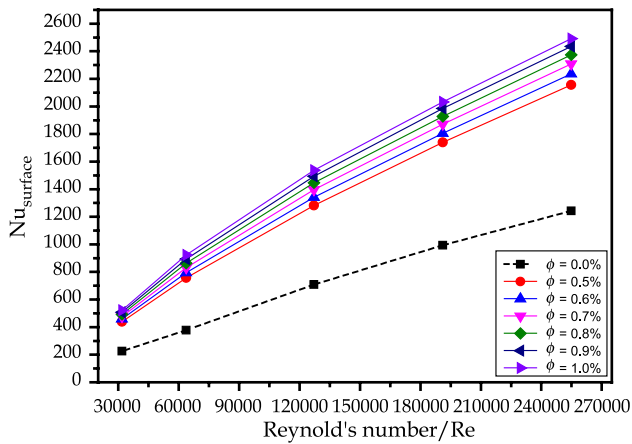


Fig. 13 Variation of surface Nusselt number with Re and addition of volume concentration of NPs

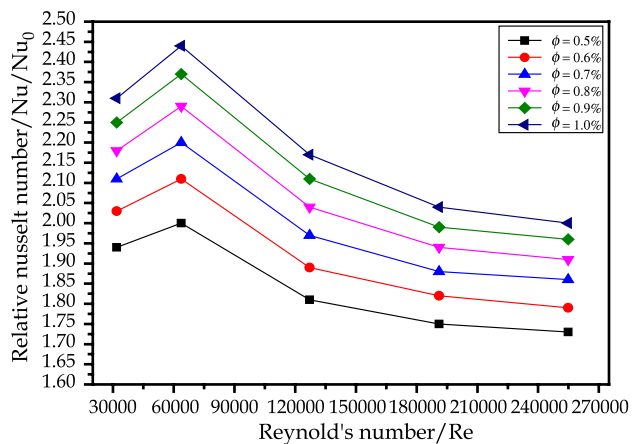


Fig. 14 Variation of relative Nusselt number with Re and addition of volume concentration of NPs

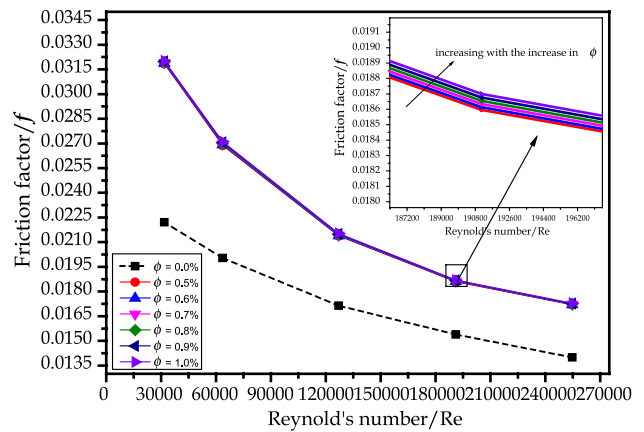


Fig. 15 Variation of friction factor with Re and addition of volume concentration of NPs

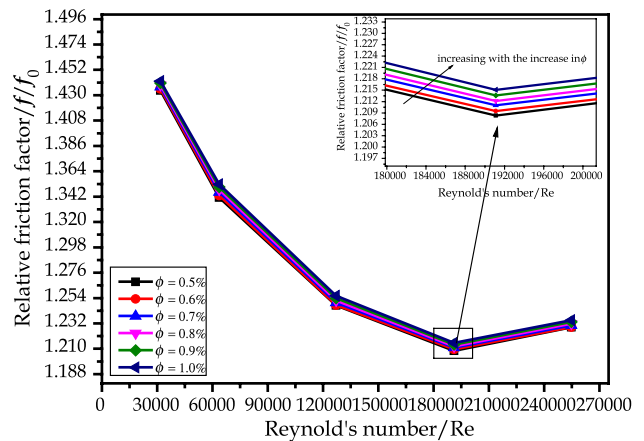


Fig. 16 Variation of relative friction factor with Re and addition of volume concentration of NPs

correlation has a value of 0.9998 and 0.9995 for R and R², respectively.

$$h = 2.6698 \times Re^{0.7389} \times \phi^{0.2485} \tag{26}$$

Correlation for surface Nusselt number (Nu_{sur})

The correlation for surface Nusselt number is given in terms of Re and ϕ in Eq. (27), which is valid for $3 \times 10^4 \leq Re \leq 2.6 \times 10^5$ and $0.5 \leq \phi \leq 1.0$. The developed correlation has a value of 0.9998 and 0.9995 for R and R², respectively.

$$Nu = 0.2541 \times Re^{0.7389} \times \phi^{0.2287} \tag{27}$$

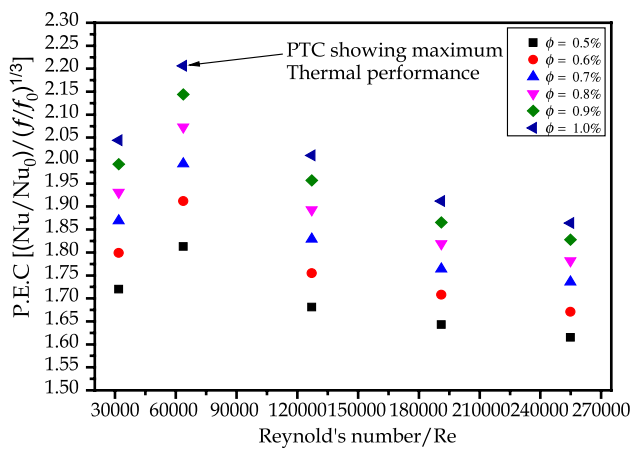


Fig. 17 Variation of PEC with Re and addition of volume concentration of NPs

Correlation for friction factor (f)

The correlation friction factor is given in terms of Re and ϕ in Eq. (28). This correlation is valid for $3 \times 10^4 \leq Re \leq 2.6 \times 10^5$ and $0.5 \leq \phi \leq 1.0$. The developed correlation has a value of 0.9974 and 0.9948 for R and R², respectively.

$$f = 0.7109 \times Re^{-0.2979} \times \phi^{0.0092} \tag{28}$$

Conclusions

A computation investigation has been carried out to propose an improved working fluid for energy transport in solar parabolic trough collectors, especially for applications requiring a high-mass flow rate. The thermofluid behavior of Fe₂O₃ nanoparticles-laden water-based nanofluid at six different volume concentrations (ϕ) ranging from 0.5 to 1.0% has been assessed. The flow Reynolds number (Re) varies between 3×10^4 to 2.6×10^5 . The heat transfer coefficient, Nusselt number, and friction factor are evaluated and compared to the base fluid. A significant enhancement in energy transport and performance evaluation criterion has been observed.

The specific heat of nanofluids decreases with the inclusion of nanoparticles, whereas the thermal conductivity increases significantly. A small but significant rise in viscosity has been observed. By doping the base fluid with 1.50% of Fe₂O₃ nanoparticles, the specific heat decreases by 4.18%, thermal conductivity increases by 6.42%, and viscosity increases by 2.56%.

At a mass flow rate of 1.5 kg s^{-1} and $\phi = 0.5\%$, a 49.21% increment in surface heat transfer coefficient was observed for nanofluid. This enhancement further rises to 57.97%

Table 3 Correlation matrix

	Re	h_{sur}	Nu_{sur}	f	ϕ
Re	1	–	–	–	–
h_{sur}	0.987634	1	–	–	–
Nu_{sur}	0.98896	0.999945	1	–	–
F	–0.95194	–0.96438	–0.96574	1	–
ϕ	0	0.123317	0.113988	0.009373	1

for nanofluid with $\phi = 1.0\%$, and the corresponding average Nusselt number rises by 59.09%. The friction factor increases with the rise in flow Reynolds number as well as nanoparticle concentration.

A performance evaluation criterion (PEC) has been employed to assess the overall efficacy of the system due to the inclusion of nanoparticles in the base fluid. A peak PEC of 2.206 was obtained at $\phi = 1.0\%$ at $Re \approx 6 \times 10^4$. In the end, correlations for surface heat transfer coefficient, friction factor, and surface Nusselt number have been proposed as a function of Reynolds number and nanoparticle volume concentration in the nanofluid.

References

1. Evangelisti L, Vollaro RDL, Asdrubali F. Latest advances on solar thermal collectors: a comprehensive review. *Renew Sustain Energy Rev.* 2019;114: 109318.
2. Rehan MA, Ali M, Sheikh NA, Khalil MS, Chaudhary GQ, ur Rashid T, et al. Experimental performance analysis of low concentration ratio solar parabolic trough collectors with nanofluids in winter conditions. *Renew Energy.* 2018;118:742–51.
3. Jebasingh VK, Herbert GMJ. A review of solar parabolic trough collector. *Renew Sustain Energy Rev.* 2016;54:1085–91.
4. Chekifi T, Boukraa M. Thermal efficiency enhancement of parabolic trough collectors: a review. *J Therm Anal Calorim.* 2022;147:10923–42. <https://doi.org/10.1007/s10973-022-11369-6>.
5. Arinze EA, Schoenau GJ, Besant RW. Thermal performance evaluation of active and passive water heat-storage schemes for solar energy applications. *Energy.* 1985;10:1215–23.
6. Padilla RV, Demirkaya G, Goswami DY, Stefanakos E, Rahman MM. Heat transfer analysis of parabolic trough solar receiver. *Appl Energy.* 2011;88:5097–110.
7. Forristall R. Heat transfer analysis and modeling of a parabolic trough solar receiver implemented in engineering equation solver. Golden: National Renewable Energy Lab; 2003.
8. Ratzel AC, Hickox CE, Gartling DK. Techniques for reducing thermal conduction and natural convection heat losses in annular receiver geometries. 1979.
9. Tao YB, He YL. Numerical study on coupled fluid flow and heat transfer process in parabolic trough solar collector tube. *Sol Energy.* 2010;84:1863–72.
10. Yılmaz İH, Mwesigye A. Modeling, simulation and performance analysis of parabolic trough solar collectors: A comprehensive review. *Appl Energy.* 2018;225:135–74.

11. Sarangi A, Sarangi A, Sahoo SS, Mallik RK, Ray S, Varghese SM. A review of different working fluids used in the receiver tube of parabolic trough solar collector. *J Therm Anal Calorim.* 2023. <https://doi.org/10.1007/s10973-023-11991-y>.
12. Choi SUS, Eastman JA. Enhancing thermal conductivity of fluids with nanoparticles. Argonne National Lab, IL (United States); 1995.
13. Mahian O, Kolsi L, Amani M, Estellé P, Ahmadi G, Kleinstreuer C, et al. Recent advances in modeling and simulation of nanofluid flows-Part I: Fundamentals and theory. *Phys Rep.* 2019;790:1–48.
14. Maxwell JC. A treatise on electricity and magnetism. Oxford: Clarendon Press; 1873.
15. Kanti P, Sharma KV, Khedkar RS, ur Rehman T. Synthesis, characterization, stability, and thermal properties of graphene oxide based hybrid nanofluids for thermal applications: experimental approach. *Diam Relat Mater.* 2022;2022:128.
16. Rashidi S, Eskandarian M, Mahian O, Poncet S. Combination of nanofluid and inserts for heat transfer enhancement: gaps and challenges. *J Therm Anal Calorim.* 2019;135:437–60. <https://doi.org/10.1007/s10973-018-7070-9>.
17. Mahian O, Kianifar A, Kalogirou SA, Pop I, Wongwises S. A review of the applications of nanofluids in solar energy. *Int J Heat Mass Transf.* 2013;57:582–94.
18. Hassani S, Saidur R, Mekhilef S, Hepbasli A. A new correlation for predicting the thermal conductivity of nanofluids; using dimensional analysis. *Int J Heat Mass Transf.* 2015;90:121–30.
19. Otanicar TP, Phelan PE, Prasher RS, Rosengarten G, Taylor RA. Nanofluid-based direct absorption solar collector. *J Renew Sustain energy.* 2010;2:33102. <https://doi.org/10.1063/1.3429737>.
20. Lu L, Liu Z-H, Xiao H-S. Thermal performance of an open thermosyphon using nanofluids for high-temperature evacuated tubular solar collectors: Part 1: indoor experiment. *Sol energy.* 2011;85:379–87.
21. Yousefi T, Veysi F, Shojaeizadeh E, Zinadini S. An experimental investigation on the effect of $\text{Al}_2\text{O}_3\text{-H}_2\text{O}$ nanofluid on the efficiency of flat-plate solar collectors. *Renew Energy.* 2012;39:293–8.
22. Yousefi T, Veysi F, Shojaeizadeh E, Zinadini S. An experimental investigation on the effect of MWCNT- H_2O nanofluid on the efficiency of flat-plate solar collectors. *Exp Therm Fluid Sci.* 2012;39:207–12.
23. Lenert A, Wang EN. Optimization of nanofluid volumetric receivers for solar thermal energy conversion. *Sol Energy.* 2012;86:253–65.
24. Zadeh PM, Sokhansefat T, Kasaiean AB, Kowsary F, Akbarzadeh A. Hybrid optimization algorithm for thermal analysis in a solar parabolic trough collector based on nanofluid. *Energy.* 2015;82:857–64. <https://doi.org/10.1016/j.energy.2015.01.096>.
25. Kasaiean A, Daviran S, Azarian RD, Rashidi A. Performance evaluation and nanofluid using capability study of a solar parabolic trough collector. *Energy Convers Manag.* 2015;89:368–75. <https://doi.org/10.1016/j.enconman.2014.09.056>.
26. Basbous N, Taqi M, Janan MA. Thermal performances analysis of a parabolic trough solar collector using different nanofluids. 2016 *Int Renew Sustain energy Conf. IEEE;* 2016. p. 322–6.
27. Bellos E, Tzivanidis C, Antonopoulos KA, Gkinis G. Thermal enhancement of solar parabolic trough collectors by using nanofluids and converging-diverging absorber tube. *Renew Energy.* 2016;94:213–22. <https://doi.org/10.1016/j.renene.2016.03.062>.
28. Iranmanesh S, Ong HC, Ang BC, Sadeghinezhad E, Esmaeilzadeh A, Mehrali M. Thermal performance enhancement of an evacuated tube solar collector using graphene nanoplatelets nanofluid. *J Clean Prod.* 2017;162:121–9. <https://doi.org/10.1016/j.jclepro.2017.05.175>.
29. Jouybari HJ, Saedodin S, Zamzamian A, Nimvari ME, Wongwises S. Effects of porous material and nanoparticles on the thermal performance of a flat plate solar collector: an experimental study. *Renew Energy.* 2017;114:1407–18. <https://doi.org/10.1016/j.renene.2017.07.008>.
30. Colangelo G, Milanese M, De Risi A. Numerical simulation of thermal efficiency of an innovative Al_2O_3 nanofluid solar thermal collector influence of nanoparticles concentration. *Therm Sci.* 2017;21:2769–79.
31. Khakrah H, Shamloo A, Hannani SK. Determination of parabolic trough solar collector efficiency using nanofluid: a comprehensive numerical study. *J Sol Energy Eng Trans ASME.* 2017;139.
32. Chamkha AJ, Selimefendigil F. Numerical analysis for thermal performance of a photovoltaic thermal solar collector with SiO_2 -water nanofluid. *Appl Sci.* 2018;8.
33. Mercan M, Yurddaş A. Numerical analysis of evacuated tube solar collectors using nanofluids. *Sol Energy.* 2019;191:167–79. <https://doi.org/10.1016/j.solener.2019.08.074>.
34. Hong K, Yang Y, Rashidi S, Guan Y, Xiong Q. Numerical simulations of a Cu-water nanofluid-based parabolic-trough solar collector. *J Therm Anal Calorim.* 2021;143:4183–95. <https://doi.org/10.1007/s10973-020-09386-4>.
35. Ashour AF, El-Awady AT, Tawfik MA. Numerical investigation on the thermal performance of a flat plate solar collector using ZnO & CuO water nanofluids under Egyptian weathering conditions. *Energy.* 2022;240.
36. Arun M, Barik D, Sridhar KP. Experimental and CFD analysis of dimple tube parabolic trough solar collector (PTSC) with TiO_2 nanofluids. *J Therm Anal Calorim.* 2022;147:14039–56. <https://doi.org/10.1007/s10973-022-11572-5>.
37. Samiezadeh S, Khodaverdian R, Doranehgard MH, Chehrmonavari H, Xiong Q. CFD simulation of thermal performance of hybrid oil-Cu- Al_2O_3 nanofluid flowing through the porous receiver tube inside a finned parabolic trough solar collector. *Sustain Energy Technol Assess.* 2022;50: 101888. <https://doi.org/10.1016/j.seta.2021.101888>.
38. Khaledi O, Saedodin S, Rostamian SH. The development of a new thermal modeling and heat transfer mechanisms of a compound parabolic concentrator (CPC) based on nanofluids. *J Therm Anal Calorim.* 2023. <https://doi.org/10.1007/s10973-023-11980-1>.
39. Dou L, Ding B, Zhang Q, Kou G, Mu M. Numerical investigation on the thermal performance of parabolic trough solar collector with synthetic oil/Cu nanofluids. *Appl Therm Eng.* 2023. <https://doi.org/10.1016/j.applthermaleng.2023.120376>.
40. Tavakoli M, Soufivand MR. Investigation of entropy generation, PEC, and efficiency of parabolic solar collector containing water/ Al_2O_3 -MWCNT hybrid nanofluid in the presence of finned and perforated twisted tape turbulators using a two-phase flow scheme. *Eng Anal Bound Elem.* 2023;148:324–35. <https://doi.org/10.1016/j.enganabound.2022.12.022>.
41. Ekiciler R, Arslan K, Turgut O. Application of nanofluid flow in entropy generation and thermal performance analysis of parabolic trough solar collector: experimental and numerical study. *J Therm Anal Calorim.* 2023;148:7299–318. <https://doi.org/10.1007/s10973-023-12187-0>.
42. Esmaeili Z, Akbarzadeh S, Rashidi S, Valipour MS. Effects of hybrid nanofluids and turbulator on efficiency improvement of parabolic trough solar collectors. *Eng Anal Bound Elem.* 2023;148:114–25. <https://doi.org/10.1016/j.enganabound.2022.12.024>.
43. Pazarlıoğlu HK, Ekiciler R, Arslan K, Adil Mohammed Mohammed N. Exergetic, Energetic, and entropy production evaluations of parabolic trough collector retrofitted with elliptical dimpled receiver tube filled with hybrid nanofluid. *Appl Therm Eng.* 2023;223.
44. Roohi R, Arya A, Akbari M, Amiri MJ. Performance evaluation of an absorber tube of a parabolic trough collector fitted with

- helical screw tape inserts using CuO/industrial-oil nanofluid: a computational study. *Sustain*. 2023;15.
45. Sokhansfat T, Kasaean AB, Kowsary F. Heat transfer enhancement in parabolic trough collector tube using Al_2O_3 /synthetic oil nanofluid. *Renew Sustain Energy Rev*. 2014;33:636–44.
 46. Kaloudis E, Papanicolaou E, Belessiotis V. Numerical simulations of a parabolic trough solar collector with nanofluid using a two-phase model. *Renew Energy*. 2016;97:218–29.
 47. Xiong Q, Bozorg MV, Doranehgard MH, Hong K, Lorenzini G. A CFD investigation of the effect of non-Newtonian behavior of Cu–water nanofluids on their heat transfer and flow friction characteristics. *J Therm Anal Calorim*. 2020;139:2601–21. <https://doi.org/10.1007/s10973-019-08757-w>.
 48. Nandan G, Wani NA. Numerical Study of Copper Oxide/Therminol VP-1 Nanofluid in Solar Parabolic Trough Collector. *Adv Eng Des*. Springer; 2021. p. 297–309.
 49. Nazir MS, Ghasemi A, Dezfulizadeh A, Abdalla AN. Numerical simulation of the performance of a novel parabolic solar receiver filled with nanofluid. *J Therm Anal Calorim*. 2021;144:2653–64.
 50. Mohammed HA, Vuthaluru HB, Liu S. Heat transfer augmentation of parabolic trough solar collector receiver's tube using hybrid nanofluids and conical turbulators. *J Taiwan Inst Chem Eng*. 2021.
 51. Karimi Y, Solaimany Nazar AR, Motevasel M. CFD simulation of nanofluid heat transfer considering the aggregation of nanoparticles in population balance model. *J Therm Anal Calorim*. 2021;143:671–84. <https://doi.org/10.1007/s10973-019-09218-0>.
 52. Alnaqi AA, Alsarraf J, Al-Rashed AAAA. Hydrothermal effects of using two twisted tape inserts in a parabolic trough solar collector filled with MgO-MWCNT/thermal oil hybrid nanofluid. *Sustain Energy Technol Assess*. 2021;47: 101331.
 53. Ekiciler R, Arslan K, Turgut O, Kurşun B. Effect of hybrid nanofluid on heat transfer performance of parabolic trough solar collector receiver. *J Therm Anal Calorim*. 2021;143:1637–54. <https://doi.org/10.1007/s10973-020-09717-5>.
 54. Babar H, Ali HM. Airfoil shaped pin-fin heat sink: Potential evaluation of ferric oxide and titania nanofluids. *Energy Convers Manag*. 2019;202: 112194. <https://doi.org/10.1016/j.enconman.2019.112194>.
 55. Chakraborty S, Panigrahi PK. Stability of nanofluid: a review. *Appl Therm Eng*. 2020. <https://doi.org/10.1016/j.applthermaleng.2020.115259>.
 56. Kim D, Kwon Y, Cho Y, Li C, Cheong S, Hwang Y, et al. Convective heat transfer characteristics of nanofluids under laminar and turbulent flow conditions. *Curr Appl Phys*. 2009;9:e119–23. <https://doi.org/10.1016/j.cap.2008.12.047>.
 57. Shah TR, Ali HM. Applications of hybrid nanofluids in solar energy, practical limitations and challenges: a critical review. *Sol energy*. 2019;183:173–203.
 58. Yuan SW. Foundations of Fluid Mechanics(Book on fluid mechanics foundations for introductory and/or secondary fluid mechanics course, with appendices containing vector analysis, inviscid fluid flow equations, etc). Englewood Cliffs: Prentice-Hall; 1967. p. 627.
 59. Yakhot V, Orszag SA, Thangam S, Gatski TB, Speziale CG. Development of turbulence models for shear flows by a double expansion technique. *Phys Fluids A Fluid Dyn*. 1992;4:1510–20.
 60. Ghasemi SE, Ranjbar AA. Effect of using nanofluids on efficiency of parabolic trough collectors in solar thermal electric power plants. *Int J Hydrogen Energy*. 2017;42:21626–34.
 61. Khanafer K, Vafai K. A critical synthesis of thermophysical characteristics of nanofluids. *Int J Heat Mass Transf*. 2011;54:4410–28.
 62. Vermahmoudi Y, Peyghambarzadeh SM, Hashemabadi SH, Naraki M. Experimental investigation on heat transfer performance of Fe_2O_3 /water nanofluid in an air-finned heat exchanger. *Eur J Mech*. 2014;44:32–41.
 63. Xuan Y, Li Q, Hu W. Aggregation structure and thermal conductivity of nanofluids. *AIChE J*. 2003;49:1038–43.
 64. Chandrasekar M, Suresh S, Bose AC. Experimental investigations and theoretical determination of thermal conductivity and viscosity of Al_2O_3 /water nanofluid. *Exp Therm Fluid Sci*. 2010;34:210–6.
 65. Brinkman HC. The viscosity of concentrated suspensions and solutions. *J Chem Phys*. 1952;20:571.
 66. Corcione M. Heat transfer features of buoyancy-driven nanofluids inside rectangular enclosures differentially heated at the sidewalls. *Int J Therm Sci*. 2010;49:1536–46.
 67. Yin P, Hasan YM, Bashar BS, AbdulZahra MM, Radhy AlKubaisy MM, Majed H, et al. Evaluation of efficiency, thermohydraulic performance evaluation criterion, and field synergy principle improvement of the parabolic solar collector containing the hybrid nanofluid using spring turbulators. *Case Stud Therm Eng*. 2023;41:102571. <https://doi.org/10.1016/j.csite.2022.102571>.
 68. Ghasemi SE, Ranjbar AA. Thermal performance analysis of solar parabolic trough collector using nanofluid as working fluid: a CFD modelling study. *J Mol Liq*. 2016;222:159–66.
 69. Petukhov BS. Heat transfer and friction in turbulent pipe flow with variable physical properties. *Adv Heat Transf*. Elsevier; 1970. p. 503–64.

Publisher's Note Springer Nature remains neutral with regard to jurisdictional claims in published maps and institutional affiliations.

Springer Nature or its licensor (e.g. a society or other partner) holds exclusive rights to this article under a publishing agreement with the author(s) or other rightsholder(s); author self-archiving of the accepted manuscript version of this article is solely governed by the terms of such publishing agreement and applicable law.